Reynolds number and slant angle effects on the flow over a slanted cylinder afterbody

Fernando Zigunov[1,†]**, Prabu Sellappan**[1] **and Farrukh Alvi**[1]

[1]Department of Mechanical Engineering, FAMU-FSU College of Engineering,
The Florida State University, Tallahassee, FL, USA

The cylinder with a slanted base is a simplified, canonical bluff body geometry that shares similarities to aircraft fuselages, which are known to produce a strong vortex pair due to their upswept afterbody. This work will examine in detail the surface flow and near-field characteristics of the flow over the slanted cylinder for slant angles of 20°, 32° and 45° with spatially dense measurements. Principal flow features of the mean flow field are identified, showing the connection between the main counter-rotating vortex pair observed in the wake and the separation bubble observed at the leading edge of the slant. A full reconstruction of the three-dimensional mean flow field using stacked stereoscopic particle image velocimetry reveals intricate details of this flow and clearly shows the direct connection between the two features. To our knowledge, this is the first direct measurement of the full three-dimensional flow topology for this geometry. The separation bubble length is found to be directly proportional to the slant angle and inversely proportional to the Reynolds number. Furthermore, the circulation within the primary vortex pair increases with increasing slant angle. This strengthening of the vortices is correlated to the form drag of this body in the vortex-dominated regime. A bi-stable steady-state wake is also observed in this flow at a low Reynolds number for the slant angle of 45°, where the formation of either a separated wake flow state or a vortex-dominated flow state is dependent upon initial conditions, i.e. the presence of overshoot of the free-stream velocity during wind tunnel start-up.

Key words: vortex interactions, wakes

1. Introduction

Aircraft fuselages are aerodynamic bluff bodies that generally feature an upswept, asymmetric afterbody at their aft ends. Practical implementation issues motivate the deviation from a more ideal axisymmetric geometry, but a fuselage drag penalty results from such a design decision. The drag increase is more pronounced for the case of military transport aircraft, where the sweep angle is generally larger to make it practical for cargo loading and payload drops during flight. It is also in this particular application that the effects of this geometry can have the most important
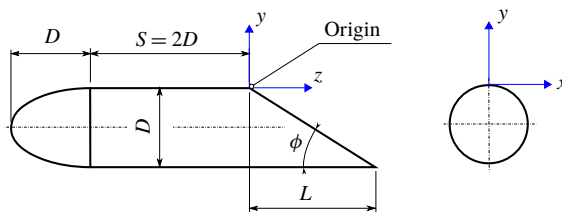
FIGURE 1. Slanted cylinder model utilized for the experiment.

negative impacts, as it is known (Britcher & Alcorn 1991; Epstein, Carbonaro & Caudron 1994) that a pair of counter-rotating vortices forms downstream of the body, which generates an upwash, from the aircraft reference frame, that generates drag and negative lift (Wortman 1999). The large moment arm of this low-pressure zone can also generate a significant pitch-up moment on the fuselage. Furthermore, the presence of the low-pressure vortex core is also a concern from the perspective of predictability and accuracy of crew and cargo drop missions, which can have their trajectories affected by the presence of the unsteady wake flow field.

A canonical geometry that is employed for the study of this flow field is the slanted cylinder, which retains the main flow topology characteristics. The slanted cylinder, represented in figure 1, consists generally of a slender axisymmetric body section that is aligned with the free stream and possesses a sharp slanted cutoff at the tail, representing the upswept afterbody of the aircraft. The slanted section is shown upside down in figure 1, when compared to the aircraft reference frame, as it also corresponds to the configuration used in this work. The presence of the sharp edge allows for experimental reproducibility and reduces the sensitivity of the flow field to boundary layer and facility characteristics, which is also useful for benchmarking of computational efforts.

The drag of the slanted cylinder was first characterized experimentally by Morel (1978), observing the effect of the slant angle (ϕ in figure 1) on the drag coefficient and sparsely measured time-resolved quantities. Morel characterized this geometry, as well as other similar bluff body geometries (such as the Ahmed body), as belonging to a group of 'critical geometries', which exhibits a sharp flow transition when one of the geometrical parameters is changed. This was readily observed experimentally in the case of the slanted cylinder as a sudden decrease in the drag as ϕ was increased. The transition occurred at $\phi \approx 47°$, which was later independently verified by Britcher & Alcorn (1991) and Xia & Bearman (1983). This transition can also be observed for different values of ϕ as a result of pitching the model, as described by Xia & Bearman (1983). Their work also demonstrated the fundamental difference between the flow patterns with smoke flow visualization, showing the quasi-periodic shedding produced by the 'fully separated wake' regime related to the low-drag state.

The high-drag state, associated with the presence of the counter-rotating vortex pair over the slanted surface, is present for the typical aircraft upsweep angles used in engineering applications, making it an interesting flow field to further explore and characterize. The vortex pair is often described as an analogue to trailing wing tip vortices (Morel 1980), however, insight into the flow field, as well as its unsteady characteristics, would only come later with the advent of full-field diagnostic techniques such as particle image velocimetry (PIV). Recently, Bulathsinghala *et al.* (2017) described this flow experimentally between $\phi = 24°$ and $\phi = 32°$ using planar

PIV, not only describing the shape of the main vortex core but also observing a potential helical mode through proper orthogonal decomposition (POD) that suggests a wandering motion of the vortices. Their observations also show a linear correlation between the slant angle and the circulation produced by the vortex formed within the range of slant angles analysed.

Studies in more realistic aircraft geometries have been conducted experimentally by many other researchers (Wortman 1999; Johnson *et al.* 2002; Bergeron *et al.* 2009; Bury, Jardin & Klöckner 2013). The PIV studies conducted by Bury *et al.* (2013) showed the effect of the curved surfaces of the simplified Lockheed Martin C-130 tail on the flow field, as well as the effects of the opening of a cargo door on the vortex trajectory. A similar study of the effect of the cargo door has recently been published in the slanted cylinder configuration by Bulathsinghala, Wang & Gursul (2019), who also observed the persistence of the vortical pair in the open configuration, although with decreased strength and increased unsteadiness levels. The effect of geometrical curvature has also been characterized in other highly three-dimensional bluff body wakes such as the Ahmed body (Rossitto *et al.* 2016, 2017), where the addition of fillets at the trailing edges of the model led to increased vortex dissipation and drag reduction. However, comparisons regarding the level of unsteadiness of these flows and vortex wandering are still to be further characterized and understood.

The extensive body of knowledge available for the Ahmed body is of relevance for the slanted cylinder flow not only because the Ahmed body wake presents a rich three-dimensional flow structure but also because it belongs to the same class of 'critical' geometries that Morel (1978) described, showing sharp flow pattern transitions as the slant angle is increased. The early work of Ahmed, Ramm & Faltin (1984) summarized the characteristics of this flow topology, identifying three main flow topologies and the mean flow structures related to each of them, some of which share similarities with the slanted cylinder with regards to the production of a vortex pair and the formation of an upper recirculation zone. One of the more recent works by Zhang, Zhou & To (2015) summarized many of the unsteady flow features present in the Ahmed body flow and showed evidence of constant or linear Strouhal scaling with Reynolds number. Similar identification of Strouhal scaling has been done by Xia & Bearman (1983) for the 'fully separated wake' (low-drag) pattern of the cylindrical body with a slanted back, pointing to a Strouhal number collapse of the wake shedding ($0.25 < St_D < 0.4$). The unsteady characteristics of the flow over the slanted cylinder, especially in the high-drag regime, are yet to be comprehensively described.

In this work, a description of the flow field over the slanted cylinder for the high-drag regime will be expanded by studying the effect of Reynolds number and slant angle. The slant angles were picked to represent more dramatic changes between the cases, making the trends in the shape of the flow structures more easily detectable. The detailed PIV measurements over a large number of spanwise planes will allow for the reconstruction of the full structure of the vortex pair and the characterization of the main features of this highly three-dimensional wake flow field.

2. Experimental set-up

2.1. *Facility and model details*

The experiments were performed in the Low Speed Wind Tunnel located at the Florida Center for Advanced Aero-propulsion (FCAAP), Florida State University. The wind tunnel has a 762 mm × 762 mm square test section that is 1.524 m long, and the free-stream turbulence levels were measured to be less than 0.3 %
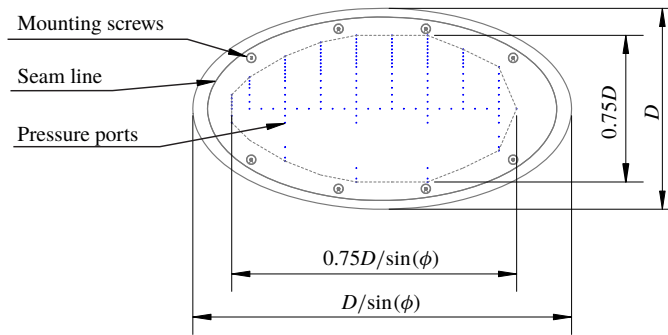
FIGURE 2. Location of the pressure ports (blue) for the $\phi = 32°$ model. Same configuration used for $\phi = 20°$ and $\phi = 45°$, scaled by the slant length L.

Re_D	$\phi = 20°$	$\phi = 32°$	$\phi = 45°$
2.5×10^4	P, 2C	P, 2C, 3C	P, 2C
4×10^4	P, 2C	P, O, 2C, 3C	P, O, 2C, 3C
2×10^5	P, O, 2C	P, O, 2C, 3C	P, O, 2C, 3C
5×10^5	P, O, 2C	P, O, 2C, 3C	P, O, 2C, 3C

TABLE 1. Experimental conditions and corresponding techniques used in this study. Legend: P = mean base pressure; O = surface oil flow; 2C = two-dimensional two-component (planar) PIV; 3C = two-dimensional three-component (stereo) PIV.

throughout the free-stream velocity range tested. Optical access is available on all four sides. The model dimensions are displayed in figures 1 and 2, and the model was manufactured out of three aluminium tubular sections, with an interchangeable rear slanted cylindrical section for the examination of different slant angles. The slanted surface was constructed with a flat aluminium plate lid cut as an ellipsoidal shape that mounted in a recessed slot of the same shape in the tubular section. The removable plate allowed the manipulation of the pressure taps during the surface pressure measurements. The mounting tolerance between the slot and the lid was ± 0.1 mm ('seam' in figure 2), having minimal effect on the flow field. The model diameter was $D = 146$ mm, and it was examined under 4 different Reynolds numbers and 3 different slant angles, totalling a set of 12 cases, which are detailed in table 1. The symbols in table 1 represent the techniques used in this study, detailed for each case.

The model nose was a half-ellipsoid of 2:1 ratio and the straight model length S was two diameters. No flow tripping device was employed during the tests, however, there is recent computational evidence (Garmann & Visbal 2019) that major disturbances and protrusions on the cylindrical surface can potentially cause a transition of the axisymmetric boundary layer. The holding strut was designed such that it would interface with the model surface at the cylindrical surface on the opposite side of the slanted surface inception, to minimize the impact of the strut on the flow physics. The strut was streamlined using a fairing with a NACA0020 airfoil shape of thickness equal to 22 mm, with the goal of reducing its effect on the flow field. To facilitate optical access to the volumes of interest, the body was placed in the tunnel upside down in relation to the aircraft reference frame, as shown in figure 3. The total
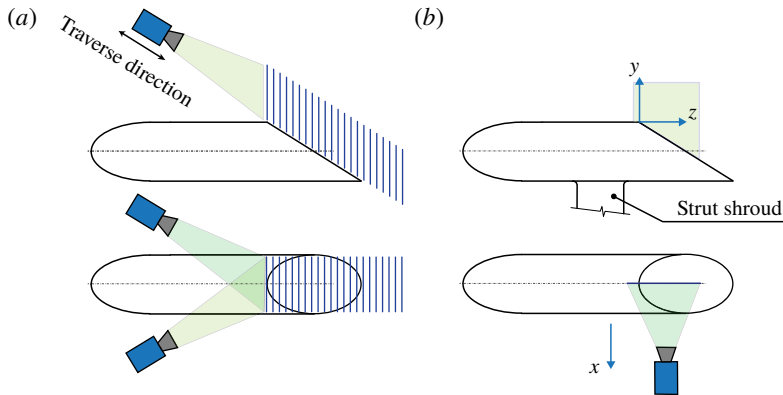
FIGURE 3. Camera and laser plane locations employed for the PIV studies. (*a*) Stereoscopic PIV set-up, (*b*) planar PIV set-up. Plane locations in (*a*) not to scale, as the locations varied with each experiment, details provided in table 3.

Re_D	Transducer range (Pa)	ΔC_p
2.5×10^4	0–24.88	0.031
4×10^4	0–24.88	0.012
2×10^5	0–248.84	0.005
5×10^5	0–2488.4	0.008

TABLE 2. Pressure transducer ranges utilized for each free-stream Reynolds number and the corresponding measurement uncertainty normalized by dynamic pressure.

blockage ratio of this model was 4.1 %, of which 2.9 % correspond to the projection of the cylindrical body aligned with the free stream and 1.2 % corresponds to the mounting strut.

2.2. *Base pressure measurements*

Average static pressure measurements were performed on the rear slanted surface at 143 pressure ports for each model slant angle, laid out as displayed in figure 2. The pressure ports were scanned using a 48-channel Scanivalve valve scanner connected to an Omega PX653 pressure transducer. The transducer range used was a function of free-stream velocity, as detailed in table 2. The maximum uncertainty in the pressure coefficients displayed in the results was $\Delta C_p = 0.03$ for the $Re_D = 2.5 \times 10^4$ case. The transducer ranges utilized for each free-stream velocity are detailed in table 2 along with the uncertainty values related to the sensors used. The measurements were averaged over 30 seconds for each port. Four runs were necessary to cover the full pressure port count, which involved stopping the tunnel fan and reconnecting the pressure tubing inside the model due to limitations in the number of pressure tubes that could be routed through the support strut. The pressure ports at the centreline remained connected throughout the pressure survey, ensuring the experiment was repeatable to within sensor uncertainty. Out of the 143 ports, 22 ports were placed at mirrored locations with respect to the *YZ* plane to validate that the mean flow was symmetric across the centre plane. Within the pressure sensor uncertainty, the same pressure values were measured in the mirrored locations for all conditions tested.

2.3. *Surface oil flow visualization*

Surface oil flow visualization was performed to understand the flow topology and to complement the PIV results. Oil flow visualization under low subsonic flow conditions proved to be challenging due to the very low shear stresses involved at the Reynolds numbers tested. A very thin layer (<0.5 mm) of clean SAE 0W5 oil was painted at the surface every run, and particles of finely ground fluorescent chalk were uniformly sprinkled over it. The slanted surface used for the oil flow runs was free of pressure port holes, to minimize the impact of these features on the observed flow patterns. Ambient lighting was significantly reduced and a set of ultraviolet (UV) lights were used to illuminate the particles to promote their fluorescence on the surface of interest. A time-lapse intervalometer was used to capture the images with a Nikon D90 camera at given delays. A 55–105 mm lens fitted with a 590 nm cutoff long-pass filter was employed to remove the blue background illumination from the UV lights. The time-lapse delay between images was 8, 15 or 30 seconds (corresponding to the three larger Reynolds numbers tested) and 20 to 50 image triplets were captured for each run. A high dynamic range colour mapping scheme was implemented by acquiring and algorithmically merging images with 1/3 s, 1 s and 3 s exposure, to enhance the contrast of the images and highlight the particle trace details such that flow features from regions with different chalk densities had similar intensity levels. While the time-lapse videos served the purpose of clarifying the direction of the movement of the seeded particles, only the last images taken will be presented herein and the flow direction will be indicated by arrows. The videos are provided as supplementary movies available online at https://doi.org/10.1017/jfm.2020.214.

2.4. *Particle image velocimetry*

2.4.1. *Stacked stereoscopic PIV (S-SPIV)*

The S-SPIV set-up consisted of two LaVision sCMOS cameras, with a resolution of 2560×2160 pixels, capturing double frames at a rate of 15 Hz. The cameras were assembled in a traversing system, shown schematically in figure 3(*a*), that was aligned with the slant angle. This was done to minimize the impact of laser reflections and improve the correlation quality close to the surface. A 200 mJ pulse^{-1}, Quantel Evergreen Nd:YAG double pulsed laser was mounted on a separate traverse that was synchronized with the cameras, to keep the laser plane in focus. The laser sheet thickness was approximately 2 mm, and the flow was seeded with propyleneglycol particles. The cameras were fitted with Scheimpflug adapters to correct for the oblique view of the laser plane. The images were acquired, de-warped and processed using the LaVision DaVis 8.4 software. The three-component velocity fields were calculated using a multi-pass cross-correlation algorithm and resulted in an in-plane vector resolution of 0.6 mm.

Several planes were acquired for the slant angles $\phi = 32°$ and $\phi = 45°$, with the precise plane locations examined described in the results section. The acquisition of a stack of multiple planes allows for the volumetric reconstruction of the mean flow, which has recently been described in detail for the wake of the Ahmed body by Sellappan, McNally & Alvi (2018), showing the trade-offs involved between performing S-SPIV versus tomographic PIV. The laser pulse energy requirement for tomographic PIV in the large wake volume was the main constraint that guided the choice towards S-SPIV to map this flow topology. The $\phi = 20°$ case was not examined under S-SPIV due to physical constraints in the optical set-up. A set of 300 image pairs was captured for each plane. In some planes, a set of 1000 images was captured to assess statistical convergence. The in-plane correlation uncertainty was typically 5 % of the local value in high-shear regions and 1 % in the free stream.

2.4.2. *Streamwise planar PIV*

Another set of PIV experiments was performed to examine the streamwise characteristics of the flow. A planar PIV set-up was employed to focus on different flow features that are difficult to resolve with the spanwise planes used in the S-SPIV data set. One LaVision sCMOS camera, along with the formerly described 200 mJ pulse^{-1} Quantel Evergreen laser, were employed to perform the image capture. A few streamwise planes were examined, however, the results shown here will be only for a plane at $x/D = 0$, (note the coordinate system in figure 3*b*), which corresponds to the centre plane. Features within the separation bubble were observed in more detail at this plane, enabling its characterization. The planar PIV sets corresponded to 500 fields captured at a rate of 10 Hz. The resulting vector fields had maximum correlation uncertainties of 1 % in regions of high shear and <0.1 % in the free stream. Additional information on the uncertainty quantification methods is given by Neal *et al.* (2015) and Wieneke (2015).

3. Results and discussion

3.1. *Surface flow features*

A representative oil flow image describing the salient flow features as observed on the surface of the slanted cylinder is displayed in figure 4. The corresponding time-lapse sequence is shown in supplementary movie 1. These features will be further characterized and confirmed by the PIV results presented in the following sections and are common between the observations made in this study.

The side view shows the oil flow tracer dragged upwards at the upwash region due to the strong suction on the slanted surface. The fluid, bounded by the cylindrical surface, collects towards the centreline and accelerates towards the slant edge along the upper portion of the cylinder. The same effect is observed in the top view of the model at the cylindrical surface close to the slant edge, where the oil flow lines converge towards the centre plane. Due to the sharp edge of the slanted surface, the shear layer location is fixed geometrically and the flow separates around the slant edge perimeter. However, the low pressure on the slanted surface causes the fluid to reattach to the surface, forming a three-dimensional, open separation bubble. The oil flow lines in the separation bubble region move upstream, as indicated by the white arrows pointing left in figure 4. The separation bubble imprints on the surface a 'source point' feature, where the oil flows outwards in all directions. The term 'source point' here will be used to refer to this particular feature observed at the reattachment of the separation bubble, however, it is to be interpreted as a typical saddle line feature observed in separation bubbles that, due to the three-dimensionality of this wake flow, is confined to a small region in space, thus appearing visually as a 'source point' in the oil flow images.

As previously described in the work of Bulathsinghala, Wang & Gursul (2016) and other researchers, this geometry's flow topology is characterized by the presence of a strong counter-rotating vortex pair, which leaves a footprint on the slanted surface as a strong sideways oil flow motion that is directed outwards from the symmetry plane and is highlighted as a dashed line in the top view of figure 4. The transition from the separation bubble to the vortex footprint is smooth. Furthermore, a secondary footprint due to a secondary vortex, which will be discussed further in § 3.3, can also be identified closer to the slant edge. These two footprints have opposite shear directions, leading to a convergence line where the oil accumulates and forms a rivulet along a line, which is labelled in figure 4 as 'Saddle line'. A similar feature
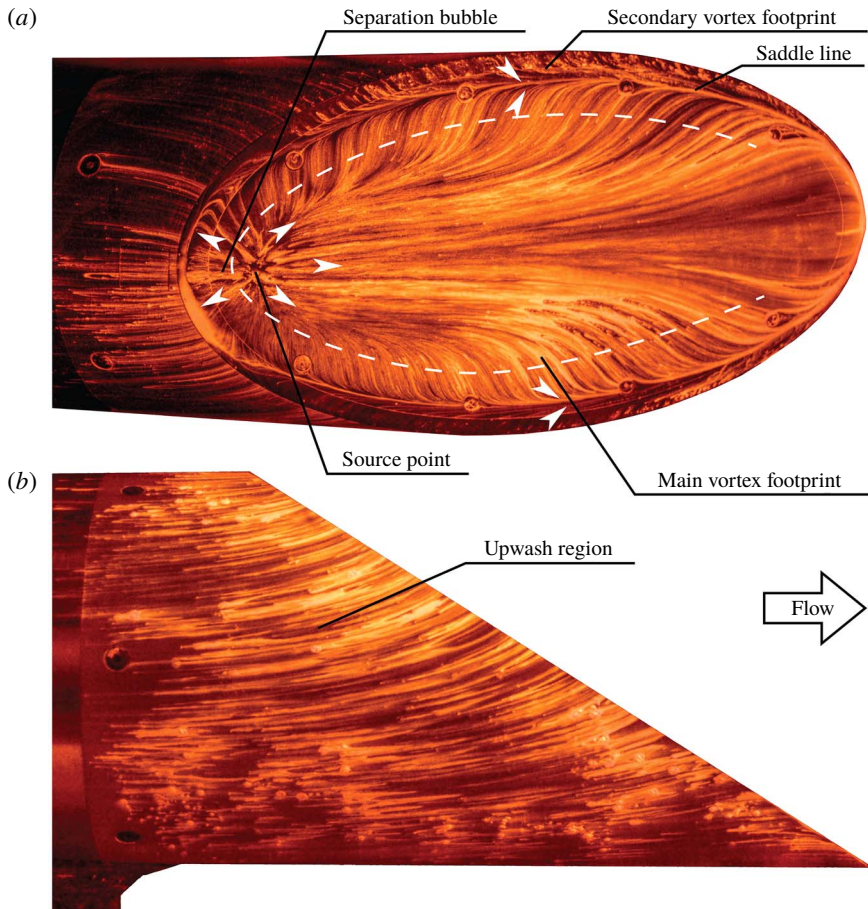
FIGURE 4. Representative oil flow image for the case $\phi = 32°$ and $Re_D = 5 \times 10^5$. Labels indicate salient flow features. White arrowheads indicate direction of oil flow. Dashed line highlights main vortex footprint. (*a*) Top view. (*b*) Side view. Corresponding time lapse is shown in supplementary movie 1.

was also observed in oil flow studies performed by Epstein *et al.* (1994) on more realistic aircraft fuselage afterbodies, which was associated with the presence of surface curvature and its effect on the vortex pair. For the slanted cylinder geometry, however, this feature can be regarded as a 'corner vortex', as it is the result of the interaction of a vortex and a shear layer at a sharp corner.

Important trends in the flow features are observed in the oil flow images shown in figure 5 as the slant angle ϕ is increased. The leading slant edge is aligned at the left side of the images to facilitate comparison of the flow feature locations. The 'source point' clearly moves downstream as the slant angle is increased, indicating a longer separation bubble. The time-lapse image sequence (supplementary movie 2) that shows the flow evolution of the $\phi = 20°$ case reveals the presence of upstream-moving oil traces, and is highlighted in the detail in figure 5. The curvature of the oil flow lines near the main vortex pair footprint location becomes more pronounced as the slant angle is increased, indicating a stronger sideways motion related to the presence of a stronger vortex. It is also observed that the spanwise extent to which the vortex
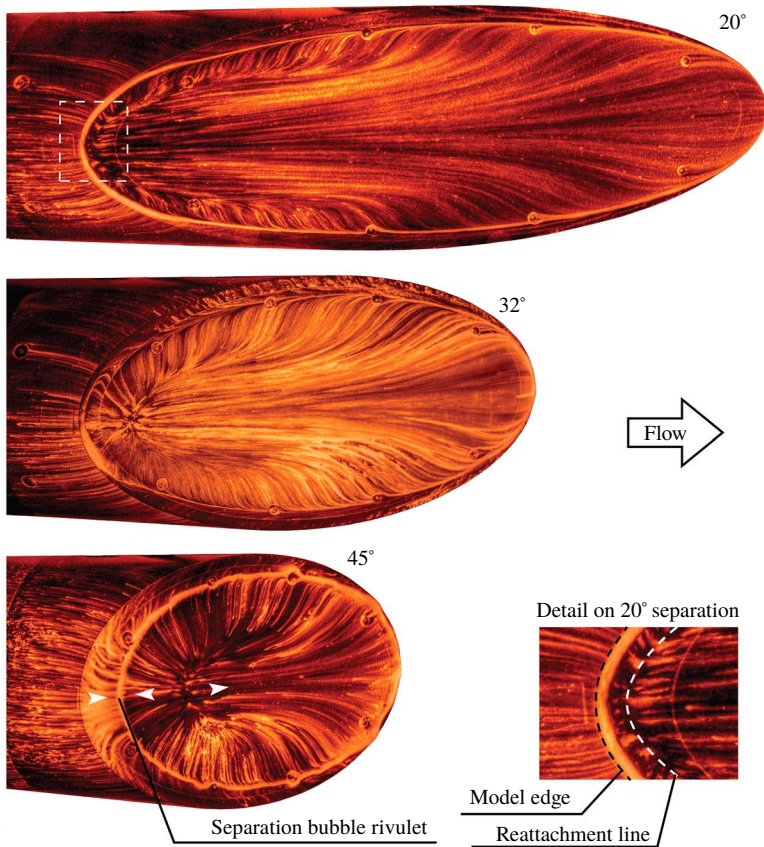
FIGURE 5. Impact of slant angle on oil flow features for $\phi = 20°$, $32°$ and $45°$. For all cases $Re_D = 5 \times 10^5$. Images show the slanted surface. Detail on $\phi = 20°$ separation bubble provided, identifying region of reversed flow (between black and white dashed lines). Time-lapse surface pattern evolution available in supplementary movies 1–3.

footprint influences the oil flow streamlines increases with slant angle ϕ, which in conjunction with the increased size of the separation bubble indicates a general trend of growth in size of relative flow features with increased slant angle.

The $\phi = 45°$ case (supplementary movie 3) presents an anomalous behaviour between the leading edge of the slanted surface at the centreline and the 'source point', where the surface lines formed a steady oil rivulet that streamed outwards towards the saddle line. The feature is labelled in figure 5 as 'Separation bubble rivulet' and the directionality of the oil flow lines is indicated with white arrows. Although it is possible that this feature could be associated with a limitation of the oil flow technique, which depends on the balance between the shear forces produced by the flow and the gravitational force acting on the oil, the PIV measurements confirm that this feature is indeed present in the mean flow field as will be discussed in § 3.5. This flow feature can be a product of the complex interaction between the separating shear layer and the reversed flow inside the separation bubble, which forms a highly unsteady flow pattern, resulting in this unusual mean downstream flow in that region.

For the 8 cases where oil flow visualization was successfully performed, it was possible to identify the reattachment point ('source point', refer to figure 4) location,
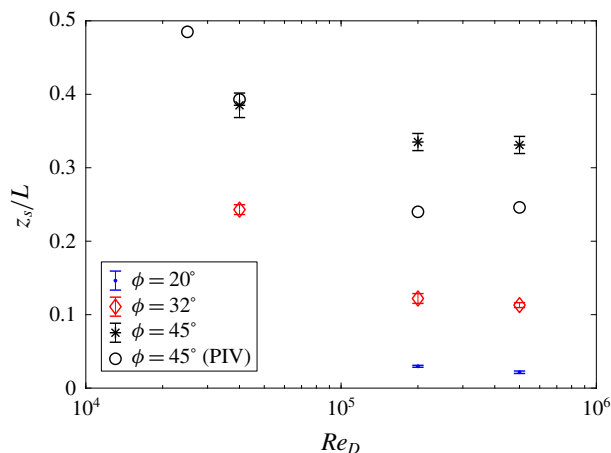
FIGURE 6. Streamwise location of the 'source point' feature as identified in the surface flow experiments as a function of Re_D and ϕ. Black circles indicate results from planar PIV for comparison.

z_s, measured from the origin. This quantity is plotted in figure 6, normalized by the slant length L. As can be observed in figure 6, the measured separation bubble lengthens (its reattachment point z_s/L moves downstream) as the Reynolds number Re_D is decreased, and the changes are significant across the order-of-magnitude changes in Re_D examined in this study. The same trend of downstream movement of the reattachment point is observed as the slant angle ϕ is increased. A comparison is provided against measured PIV reattachment locations for the $\phi = 45°$ case, and further discussion on the discrepancies observed is given in § 3.5.

3.2. *Trends in surface pressure*

Mean pressure measurements were performed at 143 pressure ports as described in § 2.2 for the 12 cases examined in this study. The trends in pressure distribution were monotonic in the vortex-dominated regime and are summarized in figure 7. The horseshoe-shaped vortex footprint described in the previous section is also observed in the pressure plots as an 'U' shape in all cases. The case shown in figure 7(i), which corresponds to $\phi = 45°$ and $Re_D = 2.5 \times 10^4$, is split in two sub-cases. This lower Reynolds number value is notable in that two different pressure signatures were possible depending on the start-up transient of the tunnel. The results for these two flow patterns observed are on either side of figure 7(i). The vastly different pressure signature indicates that this case suffered a flow pattern transition, similar to that reported by Britcher & Alcorn (1991) based on drag measurements, which were also a function of Reynolds number for this slant angle. The pressure signature shown in the right of figure 7(i) is believed to correspond to the separated wake flow pattern, whereas the left-half pressure field corresponds to the vortex pair flow pattern. Details about how the two flow patterns were obtained will be further discussed in § 3.5.

Apart from the transitional case shown in figure 7(i), the surface pressure trends are consistent with the surface flow observations. As the Reynolds number is increased, the separation bubble extent, which imparts its signature as a very low-pressure region in the surface, seems to shrink. The vortex footprint also moves towards the
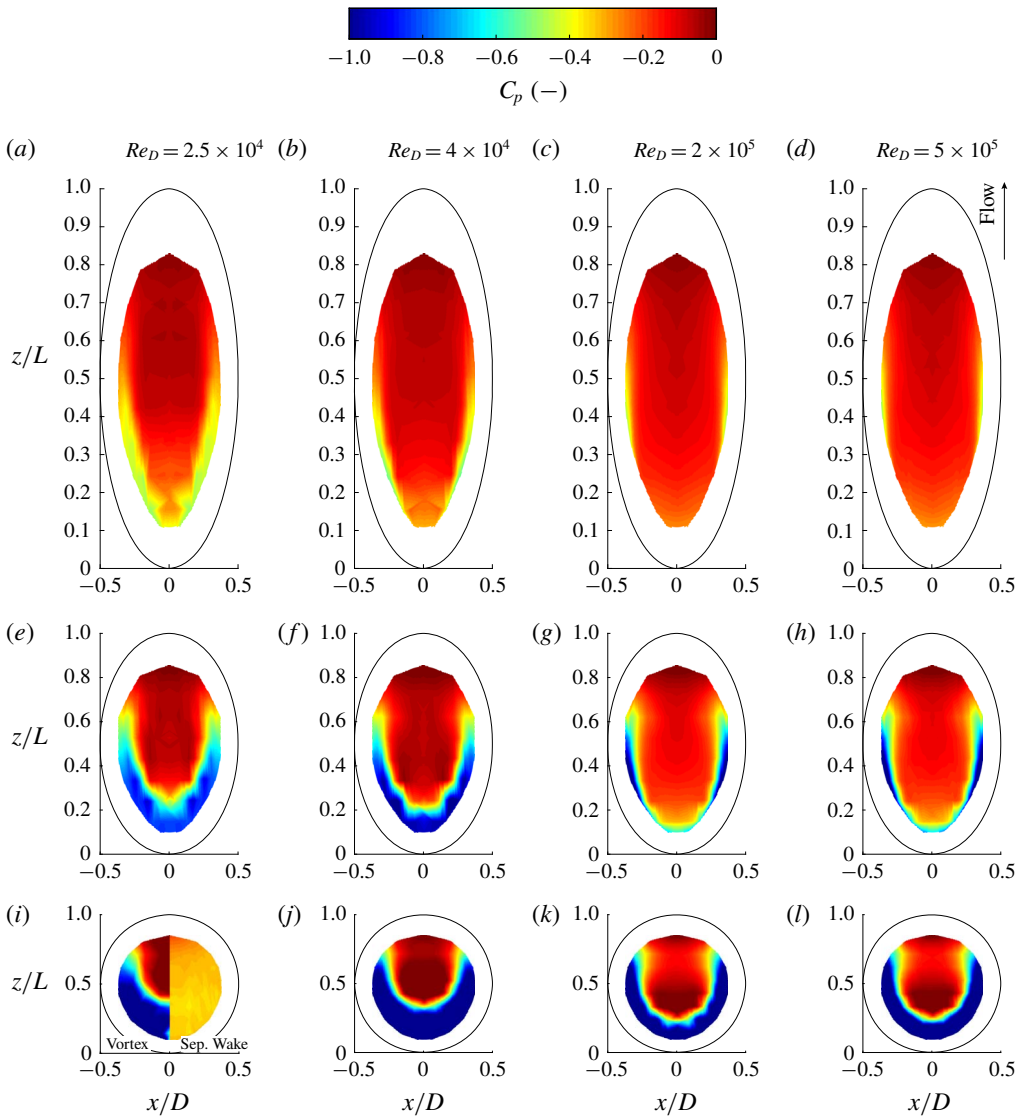
FIGURE 7. Top view showing the effect of Reynolds number and slant angle on the pressure distribution over the slanted surface for the cases studied. (*a–d*) $\phi = 20°$, (*e–h*) $\phi = 32°$, (*i–l*) $\phi = 45°$. Reynolds number indicated on the top of each column. Flow is from bottom to top.

edges of the slant, confining the extents of its influence. Due to physical construction limitations it was not possible to perform surface pressure measurements near the slanted surface edge to observe the entire vortex footprint in the pressure distribution. The inverse trend is observed when the slant angle ϕ is increased, that is, as ϕ is increased the separation bubble lengthens and the vortex footprint influences a larger portion of the slanted surface area. These trends are consistent with the observed increase in the drag coefficient C_D as the slant angle is increased as reported in past studies (Morel 1980; Xia & Bearman 1983). Since the opposite trend was observed
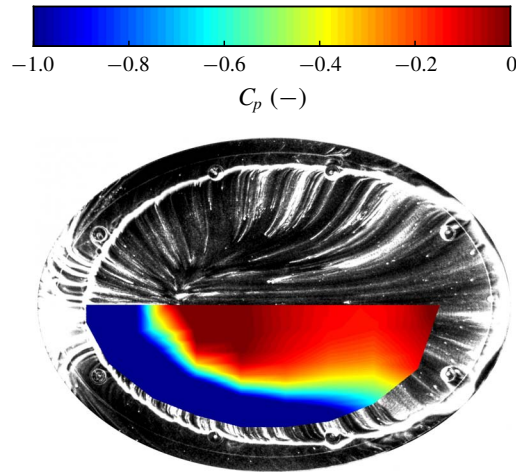
C_p $(-)$

FIGURE 8. Pressure measurements plotted against grey scale oil flow image for the $\phi = 45°$, $Re_D = 5 \times 10^5$ case, showing relative location of features. Colormap is consistent with previous figures, however, $C_{p,min} = -1.75$ exceeds colour scale.

$\phi = 32°$			$\phi = 45°$		
z_{start} (mm)	z_{end} (mm)	Δz (mm)	z_{start} (mm)	z_{end} (mm)	Δz (mm)
−1	47	3	1	40	3
47	112	5	40	120	5
112	140	7	120	170	10
140	180	10	170	215	15
180	210	15	—	—	—
210	250	20	—	—	—

TABLE 3. Resolution of the S-SPIV reconstruction performed for the $Re_D = 2 \times 10^5$ cases. Block delimiters z_{start} and z_{end} define the vector z resolution Δz within a range of z planes used for the reconstruction of the three-dimensional flow field.

with respect to Reynolds number, it is reasonable to speculate that the drag coefficient will also increase with decreasing *Re* along order of magnitude changes.

The oil flow images at the slanted surface were dewarped using a simple perspective projection based on the location of the centre of the mounting screws. The dewarped images were plotted together with the C_p measurements in figure 8 for the case $\phi = 45°$ and $Re_D = 5 \times 10^5$. The view is normal to the slanted surface. This case was specifically chosen because the 'source point' appears inside of the measurement extent of the pressure distribution. The relative position of surface flow features and their pressure signature can be correlated and it becomes evident that the recirculation region is formed due to the strong adverse pressure gradient present on the surface. The form of a horseshoe shape over the surface is consistent between the oil traces and pressure distribution.

3.3. *Three-dimensional flow topology of the near wake*

A volumetric reconstruction of the average flow field over the slant was performed for two representative cases at $Re_D = 2 \times 10^5$, with slant angles of $\phi = 32°$ and $\phi = 45°$,

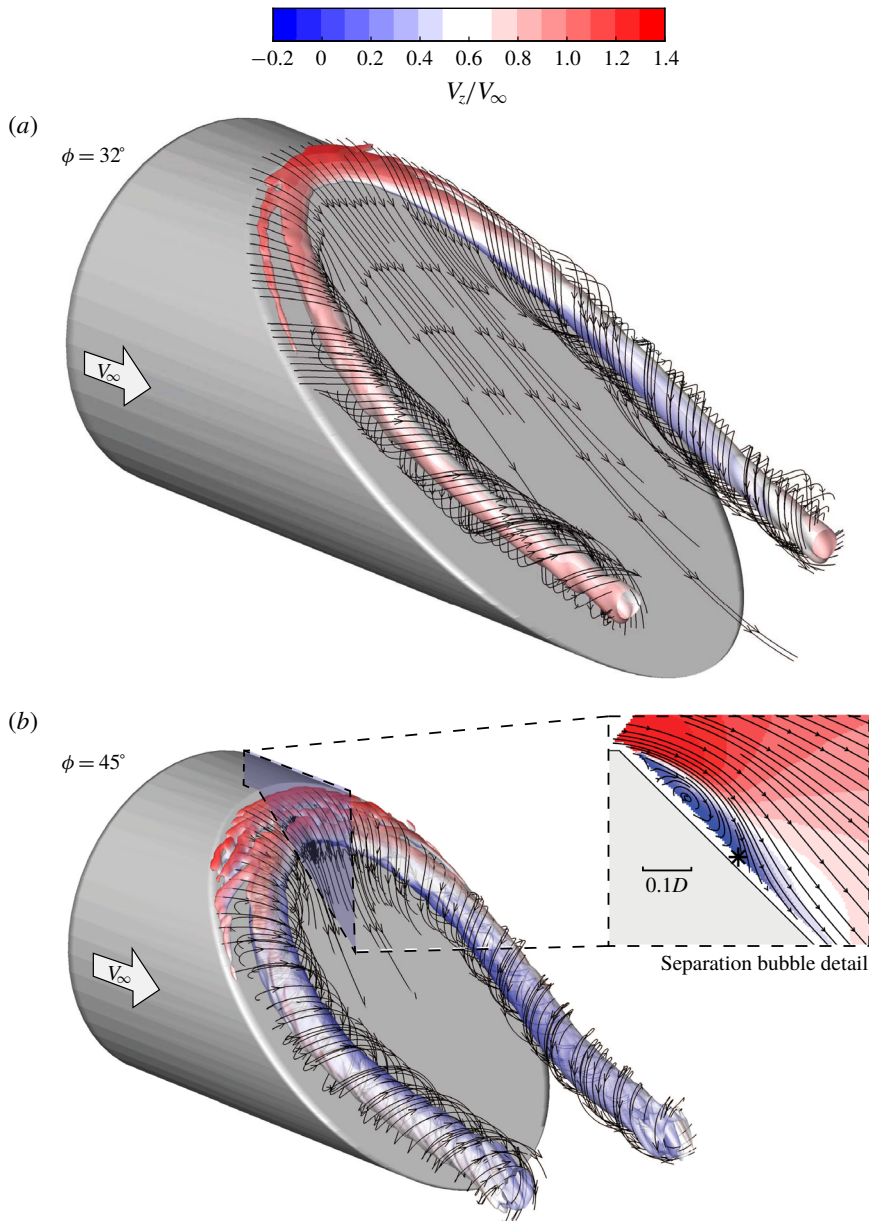FIGURE 9. S-SPIV volumetric reconstruction of the mean flow for slant angles (*a*) $\phi = 32°$ and (*b*) $\phi = 45°$, both at $Re_D = 2 \times 10^5$. Isosurfaces highlight $Q(D/V_\infty)^2 = 180$ and are coloured by non-dimensional velocity (V_z/V_∞). Streamlines seeded at approximately equally spaced points on isosurfaces of $Q(D/V_\infty)^2 = 90$ (not shown). Last plane at $z/L = 1.06$ in (*a*) and at $z/L = 1.47$ in (*b*). Inset figure shows a detail of the separation bubble recirculation zone as seen by a high magnification planar PIV experiment.

where optical access was favourable for the automated capture of multiple planes. The *z*-planes used for the reconstruction are detailed in table 3; a variable plane spacing was used to capture the fine-scale details of the flow close to the separation bubble
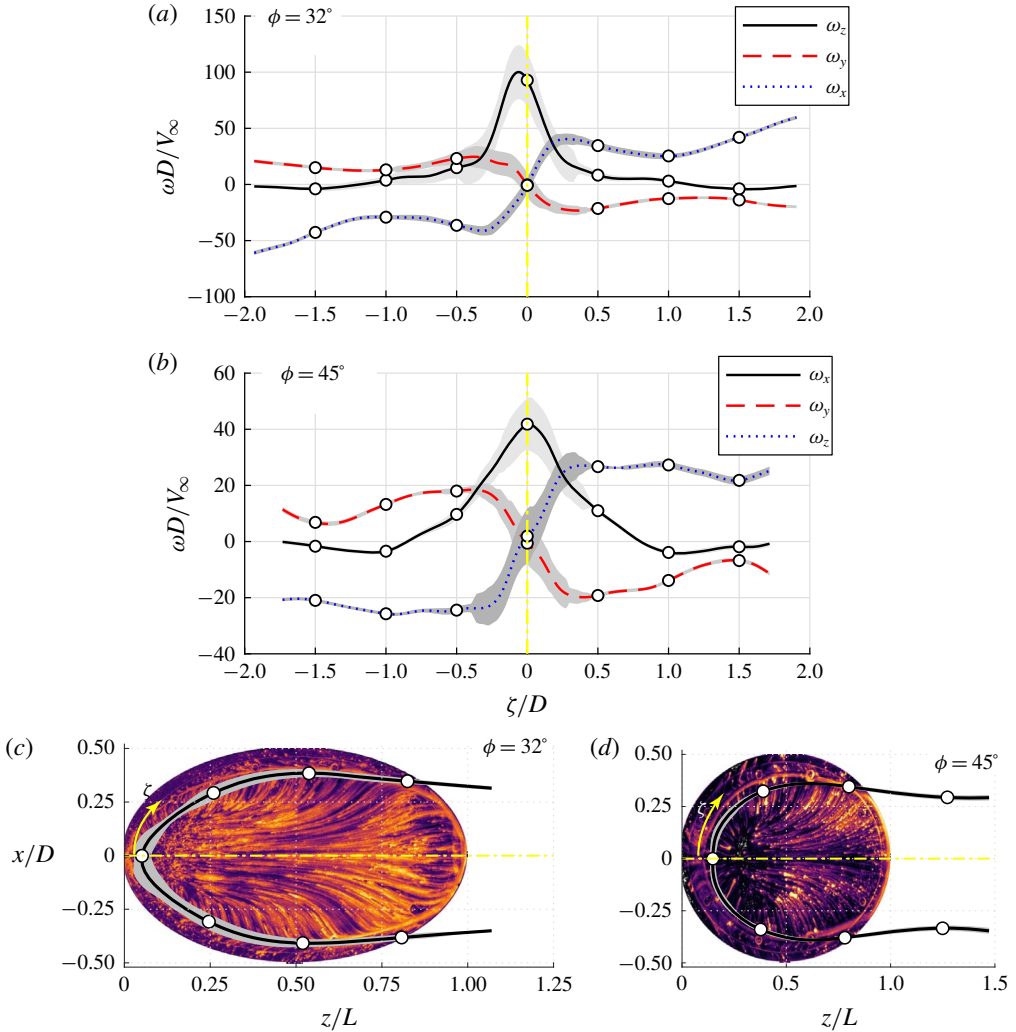
FIGURE 10. (*a,b*) Evolution of magnitude and direction of the vorticity vector components [ω_x, ω_y, ω_z] against the coordinate-transformed vortex core location ζ, as detected from the reconstructed fields of figure 9. All panels refer to $Re = 2 \times 10^5$. Mean vortex core tracking shown in (*c,d*) from local peaks of Q criterion. White circles represent matching locations in the coordinate along the vortex core ζ between left and right figures, and centreline is marked as a yellow dashed line. Corresponding oil flow photographs shown in (*c,d*) to illustrate flow pattern observed. Shaded zones represent 2σ uncertainty bounds in both vorticity quantities and vortex core location.

while avoiding the capture of an unnecessary amount of data in regions where the gradients of the quantities of interest are not as steep. Isosurfaces of dimensionless Q criterion (Hunt, Wray & Moin 1988) computed from the reconstructed mean velocity field are displayed in figure 9 to highlight the vortical structures present in the mean flow. The results presented correspond to averages of 300 PIV fields for each plane.

The isosurfaces of dimensionless Q criterion clearly highlight the dominant vortex pair in this flow, as well as the transition of the separation bubble into the vortical
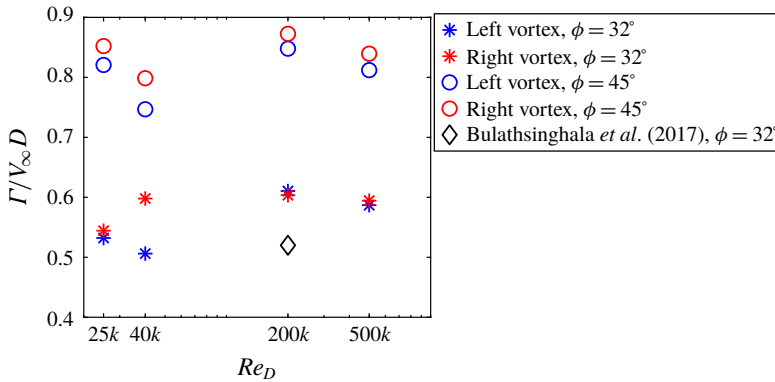
FIGURE 11. Effect of Reynolds number and slant angle ϕ on the average vortex circulation at the plane $z/L = 1.0$. Left and right vortices highlighted to show possible biases in the flow. A matching result from Bulathsinghala *et al.* (2017) is also shown for reference.

structures. This transition of the separation bubble into a pair of vortex tubes is directly measured experimentally for the first time with a high density of vectors close to the separation bubble, allowing for the adequately fine resolution of the derivative quantities necessary for computing Q in the presence of steep gradients.

The streamlines, generated from arbitrarily selected points on the isosurfaces, also reveal the vortex structure by wrapping around the isosurfaces through the measurement domain. Both slant angles reconstructed by the use of this technique present this striking transition from the inner circulation region at the separation bubble location to a free vortex pair, which indicates a very strong connection between the formation of the two structures. The lengthening of the separation bubble is also evident for the $\phi = 45°$ case. The separation feature is shown magnified in the inset figure of figure 9(*b*), showing data from the planar PIV experiment described in § 3.5. It was not possible to observe, however, a region of reversed flow for the case $\phi = 32°$ at $Re_D = 2 \times 10^5$ due to the limitations of the PIV technique close to the wall. However, based on the oil flow patterns indicating the presence of reversed flow in the surface footprint, it is reasonable to assume that the same separation bubble feature also forms for this case.

In order to quantify the connection between the separation bubble and the vortex pair, a line that goes through the local peaks in Q value was defined in the reconstructed three-dimensional vector field. This line is plotted for $\phi = 32°$ in figure 10(*c*) and $\phi = 45°$ in figure 10(*d*). A coordinate along this line, ζ, is then defined to track the vorticity quantities and their evolution as the horseshoe structure evolves downstream. The origin of this coordinate system is defined as $\zeta = 0$ when the line of local peak Q crosses the centre plane. The spanwise vorticity ω_x inside the separation bubble can then be plotted against this coordinate ζ and shown to be smoothly redirected into streamwise vorticity ω_z, as is quantitatively shown in figure 10(*a,b*) for the same cases shown in figure 9. Matching points between the vorticity charts (*a,b*) and the vortex core (*c,d*) are displayed as white circles to facilitate interpretation. The oil flow images corresponding to the same conditions display the patterns formed on the surface under the vortex core. For both slant angles examined, the centre plane location $\zeta/D = 0$ shows the peak value of spanwise
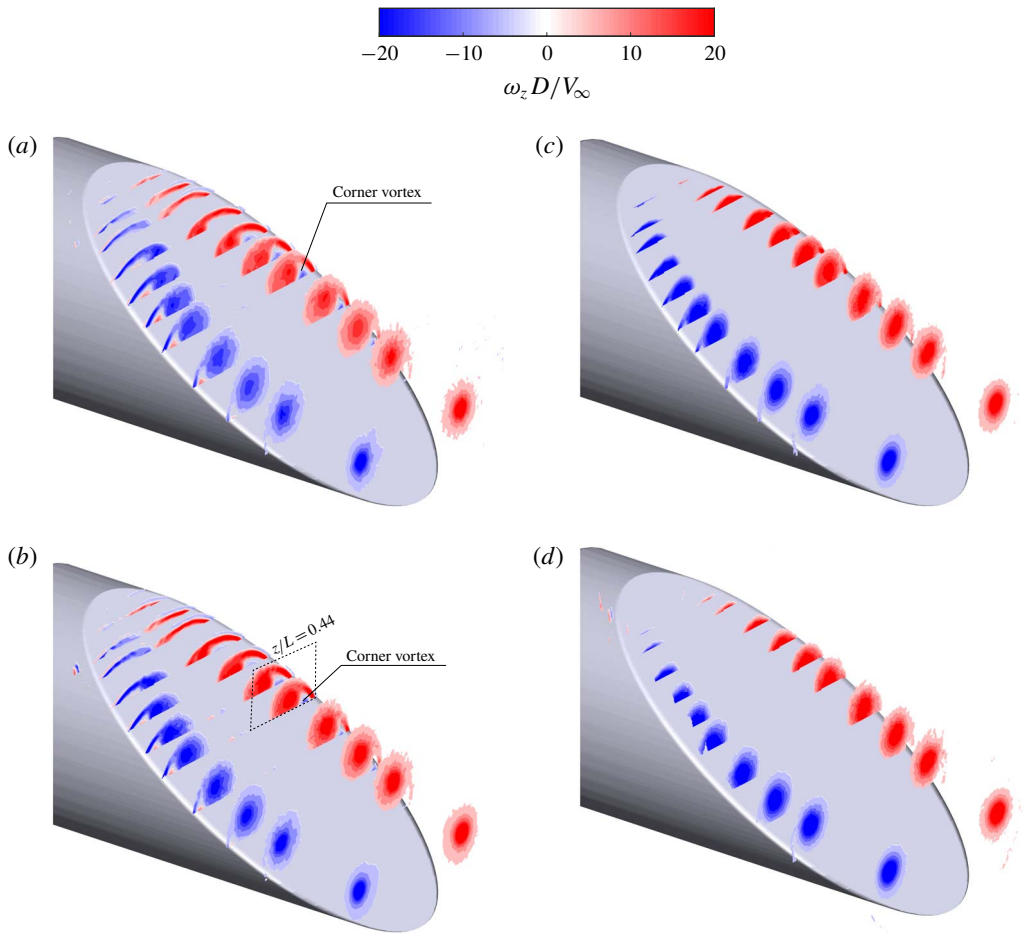
FIGURE 12. Effect of Reynolds number on the z vorticity field as observed by multiple SPIV planes. (*a*) $Re_D = 2.5 \times 10^4$, (*b*) $Re_D = 4 \times 10^4$ and (*c*) $Re_D = 2 \times 10^5$ and (*d*) $Re_D = 5 \times 10^5$ for the $\phi = 32°$ case. Absolute vorticity values $|\omega_z D/V_\infty| < 4$ occluded to highlight the important structures. Planes displayed: $z/L = 0.05$, 0.085, 0.135, 0.175, 0.25, 0.3, 0.37, 0.44, 0.54, 0.64, 0.75, 1.0.

vorticity ω_x and near-zero vertical and streamwise vorticity $[\omega_y, \omega_z]$ at the recirculation zone core. These $[\omega_y, \omega_z]$ values increase in magnitude as the vorticity vector turns streamwise and in the direction of the slanted surface. At approximately $\zeta/D = 1$, the streamwise vortex pair is fully formed, possessing non-zero $[\omega_y, \omega_z]$ as it points in the direction of the slanted surface. The extent of the interrogation volume was not sufficient to observe the free vortex pair interact ($\zeta/D > 1.5$), but it is expected that the vortices evolve asymptotically to a parallel vortex pair and eventually break down far downstream due to the Crow instability (Crow 1970).

   Trends in vortex circulation at the plane $z/L = 1.0$ are displayed in figure 11, where the normalized circulation of a single vortex is plotted for the eight cases analysed, against Reynolds number. The circulation was obtained by integrating the streamwise vorticity ω_z in circular areas of increasing radius around the peak point, until the changes in the quantity calculated were less than 2 %. In all cases, the radius of the
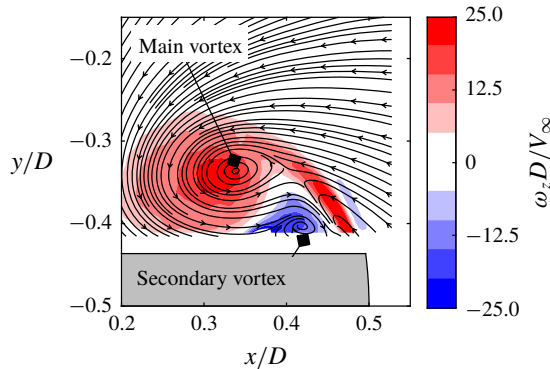
FIGURE 13. Interaction of the shear layer and the vortex, showing a counter-rotating vorticity pocket, for the $\phi = 32°$, $Re_D = 4 \times 10^4$ case. Plane at $z/L = 0.44$. Viewing axis aligned with free stream.

interrogation area was less than half the distance between the vortex cores. The circles in figure 11 point to a larger circulation for the $\phi = 45°$ case, which is on average 44 % stronger than the $\phi = 32°$ case. Comparing with figure 10(a,b), it is possible to observe that the $\phi = 32°$ case has a greater peak vorticity at the most downstream location ($\omega_z D/V_\infty > 50$) when compared with the $\phi = 45°$ case ($\omega_z D/V_\infty \approx 25$). Since the vortex with greater circulation ($\phi = 45°$) has a lower peak vorticity, it is possible to assume the case with the larger slant angle generates a less coherent vortex core, which might point to an increased wandering in relation to the $\phi = 32°$ case. Furthermore, there seems to be a slight strengthening of the vortex pair as Re_D is increased, however, the number of data points is insufficient to draw a conclusion.

The circulation of the left vortex of the $\phi = 45°$ case seems to be slightly (on average, 5 %) weaker than the right vortex, despite the experimental efforts to ensure the model was free of any yaw angle. The model centreline yaw angle was measured against the wind tunnel reference wall to be within $\pm 0.1°$ and maintained undisturbed during the entirety of this study. Asymmetry in the vector fields is also apparent in the work by Epstein *et al.* (1994), indicating this geometry may be particularly sensitive to very small changes in yaw angles with regards to the symmetry in circulation strength within the vortex flow field. The black diamond shown in the plot displays a matching case from Bulathsinghala *et al.* (2017), at $\phi = 32°$ and $Re_D = 2 \times 10^5$. Although there is disagreement in the circulation values obtained to some extent, it is not clear how the facility effect and the presence of obstacles downstream of the model will change the vortex circulation for this particular configuration. As the experiments performed in this study only employed external optical components for the PIV measurements, the effect of downstream blockage was eliminated.

A closer examination of the development of the z component of the vorticity vector, ω_z, is presented for the $\phi = 32°$ case in figure 12 for four Reynolds numbers. The lower two Reynolds number cases, (a,b), possess a noticeably different vortex shape closer to the separation bubble region in comparison to the higher Reynolds number cases, (c,d), which are indistinguishable from one another. The more elongated vorticity contours reveal a more defined shear layer at lower Re_D. By focusing on the planes around $z/L = 0.44$ (highlighted in figure 12b), a small secondary vortex (of opposite sign, labelled 'corner vortex' in figure 12) close to the slant edge can be noticed, which is also evident in the oil flow images and characterized as a 'secondary

vortex'. This secondary vorticity region seems to be related to the interaction of the main vortex and the wall, and seems to be more detectable in the lower Reynolds number cases, where the flow features are physically larger .

A detailed view of the shear layer is presented in figure 13 for the case $\phi = 32°$ and $Re = 4 \times 10^4$. The streamlines provide a means to observe the main vortex (in red) and the small counter-rotating secondary vortex (in blue). This provides evidence that this feature might be a general feature of the slanted cylinder flow topology, however, it was not possible to observe it for the higher Reynolds numbers due to the challenges related to surface reflections. However, the presence of this region at higher Reynolds numbers would explain the presence of the 'saddle line' presented in the oil flow results in figures 4 and 5, since the opposing spanwise direction of the flow over the surface forces the oil to collect in a stream. Similar evidence has been provided by Garmann & Visbal (2019) in LES simulations for $Re_D = 2 \times 10^5$ and $\phi = 28°$.

3.4. *Separation bubble and wake transition*

Planar PIV planes in the streamwise direction were captured to observe details that spanwise planes could not resolve with sufficient detail. For the $\phi = 45°$ slant angle the separation bubble was large enough to allow for the observation of its flow topology for all Reynolds numbers studied. The velocity fields obtained at the centre plane are displayed in figure 14, along with streamlines and a reattachment point location that was obtained by finding the point where the velocity parallel to the slanted surface V_s, defined in (3.1), was equal to zero.

$$V_s = V_z \cos(\phi) - V_y \sin(\phi). \tag{3.1}$$

Figure 14 also displays the trends in the separation bubble shape as Re_D is increased. The reattachment point, shown as a black star in the plots, moves upstream as Re_D is increased, following the trend observed in oil flow, as shown in figure 6. It is worth noting that although the locations z_s/L do not match, there is very good agreement on the trends observed. The oil flow measurements, due to the gravity forces acting on the oil, should be slightly biased downstream. Conversely, the reattachment location based on the PIV velocity fields by finding $V_s = 0$ should be biased upstream, especially for the higher Re_D, as the reflections from the laser sheet do not allow for observation close to the surface, and a proxy for V_s is used at the closest point measured in the field. For reference, the closest point to the surface measured from PIV is $0.015D$ from the slanted surface. Nevertheless, the very rapid growth of the separation bubble length as Re_D is decreased is a potential explanation for the transition of this flow to a fully separated wake pattern at lower Reynolds numbers.

The flow topology within the separation bubble, however, is complex. It is more evident in the lower Reynolds number cases in figure 14(a,b), for which the larger physical size of the separation bubble allowed for the observation of the details of the flow. The streamlines separate first at the sharp edge as expected, however, a mean forward flow is observed close to the surface. This 'mean forward flow region' indicated in figure 14(a) has a very low velocity magnitude but also very low shear stresses. The mean velocity gradients remain concentrated in the shear layer. The reattachment pattern seems to separate once again, which happens at $z/L = 0.24$ for the $Re_D = 2.5 \times 10^4$ case, this time forming a recirculation zone. The flow then reattaches for the last time where the black star is plotted. This unusual separation bubble pattern seems to be corroborated by the surface flow pattern discussed in § 3.1.
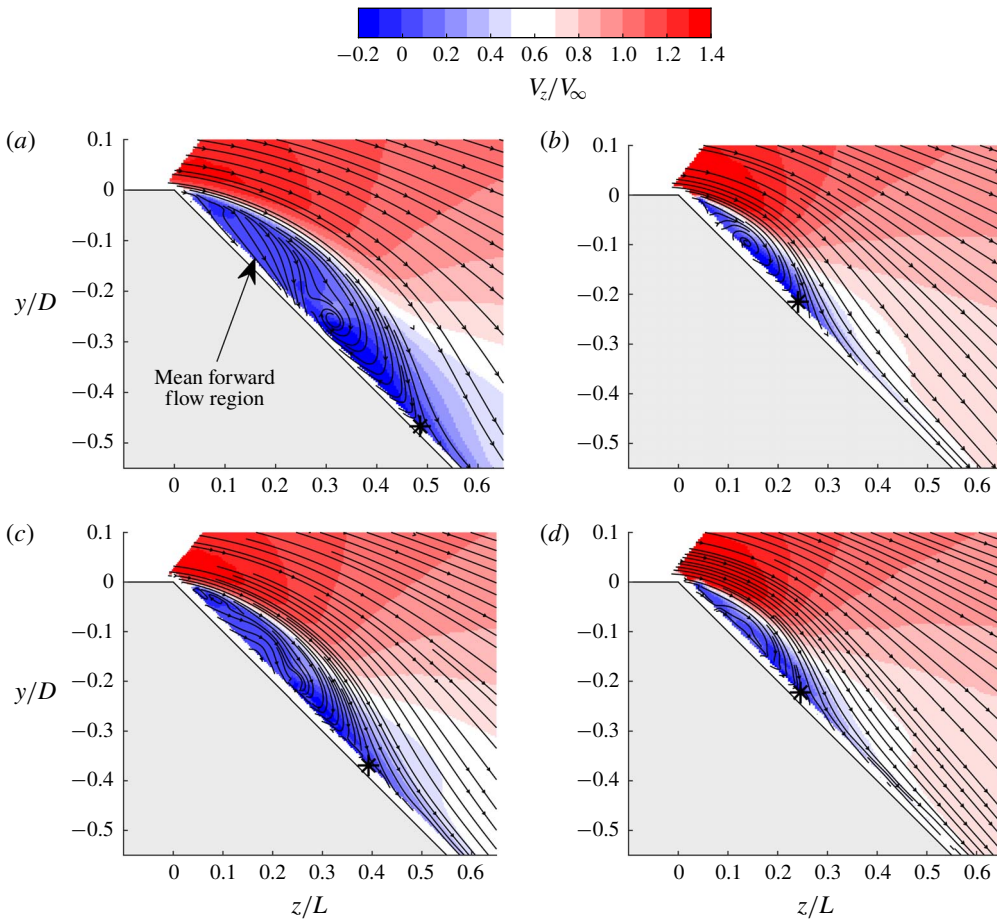
FIGURE 14. Effect of Re_D on the separation bubble shape as seen through contours of normalized streamwise velocity calculated from the mean of 500 planar PIV fields at $x/D = 0.0$ for $\phi = 45°$ and (a) $Re_D = 2.5 \times 10^4$, (b) $Re_D = 4.1 \times 10^4$, (c) $Re_D = 2 \times 10^5$, (d) $Re_D = 5 \times 10^5$. Black star shows the reattachment point computed as $V_s = 0$.

It is conjectured here that this unusual separation feature shape is a product of a highly three-dimensional interaction in the flow field. The oil flow pattern between the sharp edge and the 'Separation bubble rivulet' feature shown in figure 5 suggests that there is average flow towards the centre plane, indicating the mean streamlines sharply deflect from the sides of the cylindrical surface towards the centre plane as soon as they reach the slanted edge, potentially due to a very steep pressure gradient. Future studies of the topology details in this region might lead to a clearer picture of the global flow pattern transitional characteristics and their connection with the incoming boundary layer characteristics. This separation bubble feature has not been identified in the $\phi = 20°$ and $\phi = 32°$ cases due to limitations in the spatial resolution of the optical equipment used, and therefore require a specially designed experiment to achieve the necessary magnification levels.

The flow topology at the lower Reynolds number for the $\phi = 45°$ case proved to be bi-stable in steady state. As can be observed in figure 15, there are two possible flow states for the same Reynolds number of $Re_D = 2.5 \times 10^4$. The transition is apparently
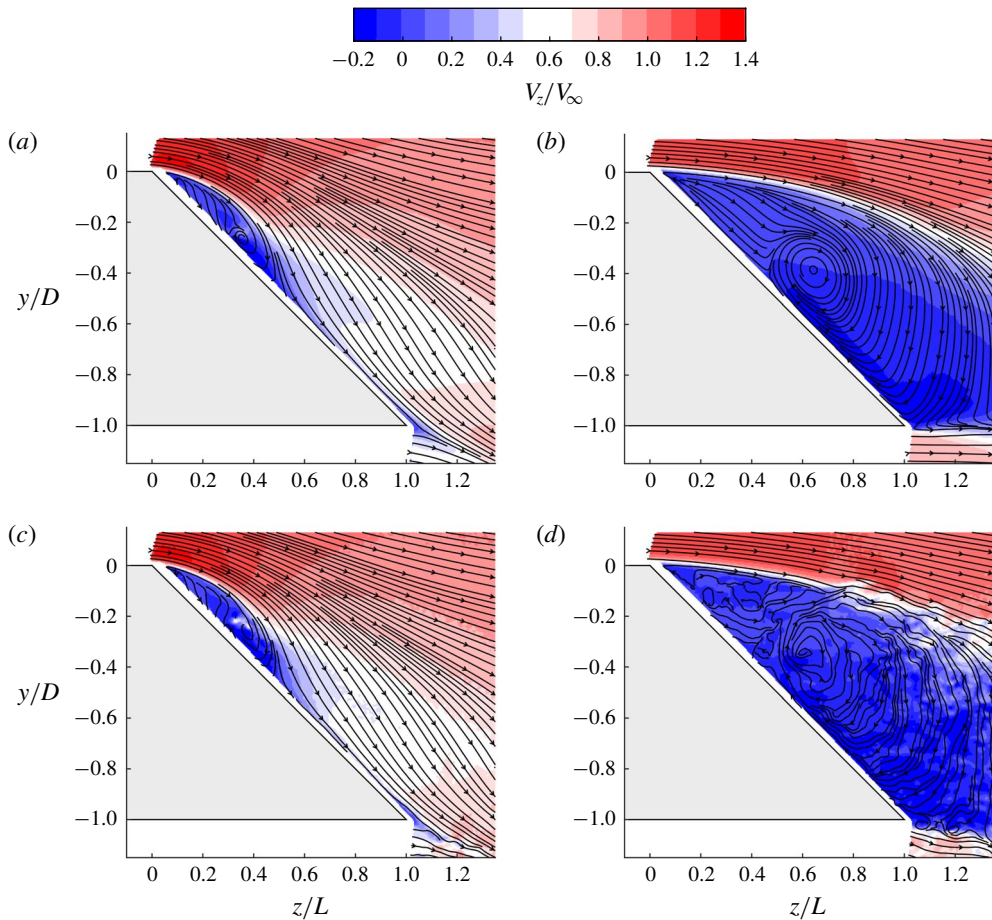
FIGURE 15. Steady-state bi-stability of the case $Re_D = 2.5 \times 10^4$ and $\phi = 45°$ at centre plane ($x/D = 0.00$). In (*a*) the separation bubble closes inside the slanted surface, which is related to the formation of a counter-rotating vortex pair. In (*b*) the open separation pattern is related to a more unsteady wake. (*c*,*d*) Representative instantaneous snapshots of the corresponding cases (*a*,*b*).

related to the hysteresis effect first related by Britcher & Alcorn (1991) in a model with the same slant angle based on drag and base pressure measurements. The flow state in figure 15(*a*) shows a closed separation bubble and is believed to be related to the formation of the pair of counter-rotating vortices over the slanted surface given the S-SPIV results presented for the higher Reynolds number cases.

The flow state shown in figure 15(*b*) corresponds to what is regarded in the literature as a fully separated wake pattern. The two flow fields possess the same free-stream velocity as measured by a Pitot-static probe upstream of the model. The vortex flow state in figure 15(*a*) can be attained, with consistent repeatability, by letting the free-stream velocity overshoot to a higher value (in this experiment, to $Re_D = 4 \times 10^4$ or $V_\infty = 4.1$ m s^{-1}) and then reducing it to the corresponding 2.6 m s^{-1} ($Re_D = 2.5 \times 10^4$). The wake flow state in (*b*), however, can only be obtained if the free-stream velocity is slowly increased to 2.6 m s^{-1} without overshoot. The maximum acceleration rates were limited by the facility control systems to 0.7 m s^{-2}.
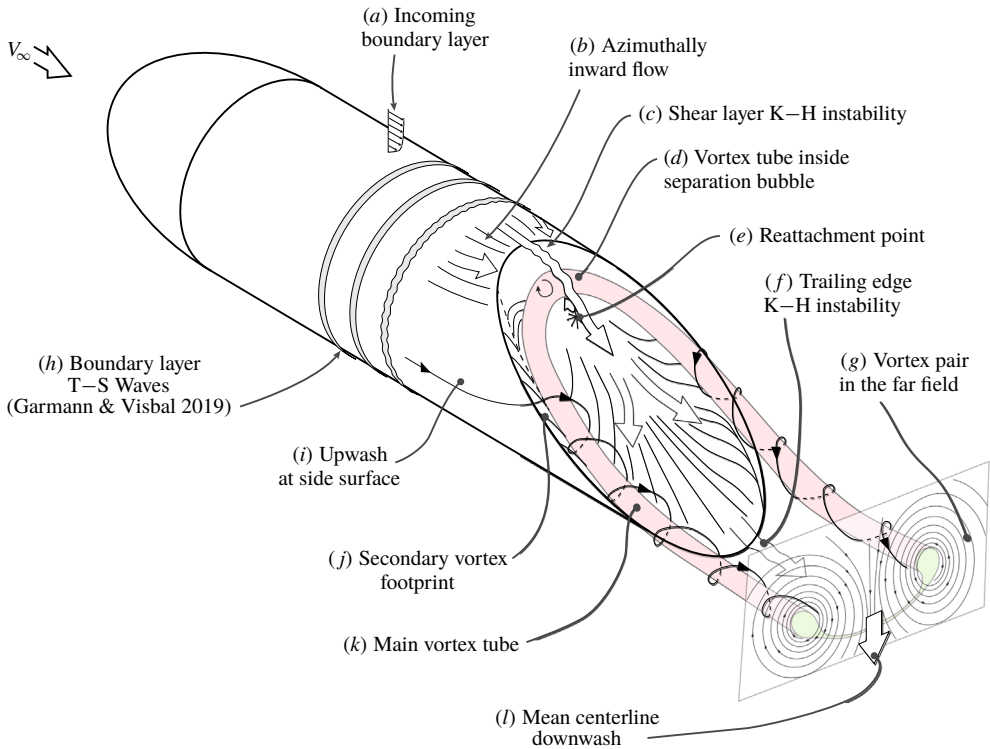
FIGURE 16. Schematic summarizing the three-dimensional features of the general vortex-dominated regime of the flow over a cylinder with a slanted afterbody. These flow features are believed to be encountered over a large range of Re_D and ϕ.

The instantaneous snapshots shown in figure 15(c,d) reveal the finer-scale flow structures that compose both flow states. The wake state observed in figure 15(d) shares similarities with the flow visualization photographs shown by Xia & Bearman (1983) for $\phi = 70°$, potentially indicating the slant angle of $\phi = 45°$ would also display a low-frequency shedding mode when transitioned to the wake state. It is clear, however, that the fluctuations in the vortex state in figure 15(c) are much lower in magnitude with respect to the mean when compared to the wake state of figure 15(d).

Based on these observations, it is proposed herein that the vortex flow pattern is the preferred flow state in this bi-stable wake. Both flow states persisted for as long as the experiments lasted (10 min, or $V_\infty t/D > 10^4$), providing strong indication that both states are stable indefinitely, even though the wake state might present strong shedding dynamics. Once a coherent vortex pair is formed through the overshoot of free-stream velocity, their net induced velocity at the centre plane deflects the free-stream streamlines towards the slanted surface and enables the separation bubble to reattach in the slanted surface. This deflection of the free stream enables the vortex dominated wake to persist even after the Reynolds number has been lowered.

3.5. *Summary of the vortex-dominated wake structure*

Building on the results shown by past researchers and the observations performed in this study, it is possible to compile the major flow structures present in the general

flow over the slanted cylinder geometry in a generic sketch. A schematic of the flow structures identified for the vortex-dominated wake pattern is presented in figure 16 and adds detail to the sketches presented by Morel (1980) and Britcher & Alcorn (1991). Based on the observations presented in this work, the features shown in figure 16 are expected to be common to a large range of slant angles and Reynolds numbers where the vortex-dominated wake pattern is present.

The influence of the vortex-dominated wake is observed upstream at the cylindrical section as an azimuthally inward cross-flow at the boundary layer close to the slant leading edge (figure 16*b*). The incoming boundary layer at the cylindrical section (*a*) is subject to an instability similar to the Tollmien–Schlichting waves (*h*), as observed in the computational work of Garmann & Visbal (2019). Depending on the incoming turbulence and fineness ratio of the cylindrical body, transition to a turbulent boundary layer might occur. When the sharp edge of the slanted surface is reached, a shear layer forms, which is subject to the Kelvin–Helmholtz (K–H) instability (*c*). The separation bubble closes at the reattachment point, forming a circulation zone inside of it. This circulation zone was found to be continuously connected (*d*) to the vortex tube pair in the far wake (*g*), forming a horseshoe-shaped vortical structure that can be observed in the mean flow.

The effects of the low pressure caused by the horseshoe vortex also extend upstream along the cylindrical surface, causing an upwash (*i*). Under the main vortex tube (*k*) a secondary vortex-like structure (*j*) arises from the formation of the shear layer at that location. The shear layer at the trailing edge (*f*) is also subject to a K–H type instability due to the mismatch between flow velocity along the upper and lower surfaces at the trailing edge. The induced velocity from the vortex pair causes a mean downwash at the centreline (*l*) that draws the freely interacting vortex pair down, until their breakdown. This general flow topology is universal over a wide range of Re_D and ϕ.

4. Conclusions

In this experimental work, a detailed description of the flow field over the slanted cylinder over a wide range of Reynolds numbers and slant angles was provided. Oil flow images, together with a stacked SPIV flow field reconstruction, enabled the definition of the main features that are common to all cases experimented. A 'horseshoe vortex' feature, which is the result of a smooth transition between a separation bubble and a pair of counter-rotating vortices, is the most striking feature observed. Its presence causes a very low-pressure region over the slant plane, which has an effect on the flow over the cylindrical surface that is seen as a large acceleration both towards the centre plane and towards the slanted surface. The footprint of a secondary vortex was also observed, whose existence and shape were confirmed by PIV measurements.

The experimental observations provided in this work provide evidence that as the slant angle is increased, the separation bubble grows in size and the vortices increase in circulation, becoming stronger. It is conjectured from these observations that when the separation bubble grows to a length comparable to the length of the slanted surface, the flow transitions to the fully separated wake state. The effect of lengthening of the separation bubble was also observed as the Reynolds number is decreased, however, it is unclear if the same trend applies to vortex strength. As far as the data points analysed can show, the vortex strength trends are much less prominent than the trends in separation bubble length with respect to Reynolds number.

The separation bubble shape for $\phi = 45°$ was also characterized. The flow pattern observed suggests the presence of a highly three-dimensional flow field inside the separation bubble, potentially indicating the presence of an inflow from off-centre locations towards the centre. Furthermore, a bi-stable flow pattern was observed at the lower Reynolds number $Re_D = 2.5 \times 10^4$ for the $\phi = 45°$ model, related to the initial overshoot of free-stream velocity. It is very likely that other means could be used to cause the switching of flow patterns, opening up the possibility for active flow control studies for this geometry. Lastly, a schematic is presented summarizing the flow features over this canonical bluff body, compiling the features that are common to the vortex-dominated wake flow regime of the cylinder with a slanted base.

Declaration of interests

The authors report no conflict of interest.

Supplementary movies

Supplementary movies are available at https://doi.org/10.1017/jfm.2020.214.

REFERENCES

AHMED, S. R., RAMM, G. & FALTIN, G. 1984 Some salient features of the time-averaged ground vehicle wake, *Tech. Rep.* SAE Technical Paper.

BERGERON, K., HAYES, M., ARONOFF, J. & CHARLES, R. 2009 C-17 low speed wind tunnel wake-vortex study. *AIAA Paper* 2009–1482.

BRITCHER, C. P. & ALCORN, C. W. 1991 Interference-free measurements of the subsonic aerodynamics of slanted-base ogive cylinders. *AIAA J.* **29** (4), 520–525.

BULATHSINGHALA, D., WANG, Z. & GURSUL, I. 2016 Effect of upsweep angle on afterbody vortices. In *46th AIAA Fluid Dynamics Conference*, pp. 1–25.

BULATHSINGHALA, D., WANG, Z. & GURSUL, I. 2019 Modified near-wakes of axisymmetric cylinders with slanted base. *Aerosp. Sci. Technol.*

BULATHSINGHALA, D. S., JACKSON, R., WANG, Z. & GURSUL, I. 2017 Afterbody vortices of axisymmetric cylinders with a slanted base. *Exp. Fluids* **58** (5), 1–24.

BURY, Y., JARDIN, T. & KLÖCKNER, A. 2013 Experimental investigation of the vortical activity in the close wake of a simplified military transport aircraft. *Exp. Fluids* **54** (5), 1524.

CROW, S. 1970 Stability theory for a pair of trailing vortices. *AIAA J.* **8**, 2172–2179.

EPSTEIN, R. J., CARBONARO, M. C. & CAUDRON, F. 1994 Experimental investigation of the flowfield about an upswept afterbody. *J. Aircraft* **31** (6), 1281–1290.

GARMANN, D. J. & VISBAL, M. R. 2019 High-fidelity simulations of afterbody vortex flows. *AIAA J.* **57** (9), 3980–3990.

HUNT, J. C., WRAY, A. A. & MOIN, P. 1988 Eddies, streams, and convergence zones in turbulent flows. In *Proc. 1988 Summer Program Cent. Turbul. Res.*, pp. 193–207. Center for Turbulence Research, Stanford, CA.

JOHNSON, W., TRICKEY, C., FORSYTHE, J., ALBERTSON, J. & LEIGH, E. 2002 Experimental and computational investigation of the flow behind a C-130 with tailgate down. In *40th AIAA Aerospace Sciences Meeting and Exhibit,* Reno, NV.

Morel, T. 1978 *The Effect of Base Slant on the Flow Pattern and Drag of Three-Dimensional Bodies with Blunt Ends*. Springer.

Morel, T. 1980 Effect of base slant on flow in the near wake of an axisymmetric cylinder. *Aeronaut. J.* **31** (2), 132–147.

Neal, D., Sciacchitano, A., Smith, B. & Scarano, F. 2015 Collaborative framework for piv uncertainty quantification: the experimental database. *Meas. Sci. Technol.* **26** (7), 074003.

Rossitto, G., Sicot, C., Ferrand, V., Borée, J. & Harambat, F. 2017 Aerodynamic performances of rounded fastback vehicle. *Proc. Inst. Mech. Engrs* D **231** (9), 1211–1221.

Rossitto, G., Sicot, C., Ferrand, Vérie, Borée, J. & Harambat, F. 2016 Influence of afterbody rounding on the pressure distribution over a fastback vehicle. *Exp. Fluids* **57** (3), 43.

Sellappan, P., McNally, J. & Alvi, F. S. 2018 Time-averaged three-dimensional flow topology in the wake of a simplified car model using volumetric PIV. *Exp. Fluids* **59** (8), 124.

Wieneke, B. 2015 PIV uncertainty quantification from correlation statistics. *Meas. Sci. Technol.* **26** (7), 074002.

Wortman, A. 1999 Reduction of fuselage form drag by vortex flows. *J. Aircraft* **36** (3), 501.

Xia, X. & Bearman, P. 1983 An experimental investigation of the wake of an axisymmetric body with a slanted base. *Aeronaut. Q.* **34** (1), 24–45.

Zhang, B. F., Zhou, Y. & To, S. 2015 Unsteady flow structures around a high-drag Ahmed body. *J. Fluid Mech.* **777**, 291–326.